PNAS RESEARCH ARTICLE | BIOPHYSICS AND COMPUTATIONAL BIOLOGY

Exploiting the intrinsic misfolding propensity of the KRAS oncoprotein

Kobe Janssen[a,b], Filip Claes[c], Dido Van de Velde[c], Vanessa L. Wehbi[c], Bert Houben[a,b], Yulia Lampi[a,b], Mieke Nys[a,b], Laleh Khodaparast[a,b], Ladan Khodaparast[a,b], Nikolaos Louros[a,b], Rob van der Kant[a,b], Joffre Verniers[a,b], Teresa Garcia[a,b], Meine Ramakers[a,b], Katerina Konstantoulea[a,b], Katerina Maragkou[a,b], Ramon Duran-Romaña[a,b], Mónica Musteanu[d,e,f], Mariano Barbacid[d,f], Bernard Scorneaux[c], Els Beirnaert[c], Joost Schymkowitz[a,b,1], and Frederic Rousseau[a,b,1]

Edited by Lila Gierasch, University of Massachusetts Amherst, Amherst, MA; received September 2, 2022; accepted January 18, 2023

Mutant KRAS is a major driver of oncogenesis in a multitude of cancers but remains a challenging target for classical small molecule drugs, motivating the exploration of alternative approaches. Here, we show that aggregation-prone regions (APRs) in the primary sequence of the oncoprotein constitute intrinsic vulnerabilities that can be exploited to misfold KRAS into protein aggregates. Conveniently, this propensity that is present in wild-type KRAS is increased in the common oncogenic mutations at positions 12 and 13. We show that synthetic peptides (Pept-ins™) derived from two distinct KRAS APRs could induce the misfolding and subsequent loss of function of oncogenic KRAS, both of recombinantly produced protein in solution, during cell-free translation and in cancer cells. The Pept-ins exerted antiproliferative activity against a range of mutant KRAS cell lines and abrogated tumor growth in a syngeneic lung adenocarcinoma mouse model driven by mutant KRAS G12V. These findings provide proof-of-concept that the intrinsic misfolding propensity of the KRAS oncoprotein can be exploited to cause its functional inactivation.

KRAS | oncogene | protein aggregation | protein folding | peptide

Globular proteins consist of secondary structural elements that are packed through hydrophobic interactions that stabilize its tertairy structure. This particular architecture imposes constraints on the primary structure of natural proteins resulting in the occurrence of hydrophobic segments along the primary structure. While essential for protein stability, these segments constitute intrinsic vulnerabilities on the folding landscape of globular proteins as they are also prone to protein misfolding and aggregation. Indeed, these aggregation-prone regions (APR) (1, 2) also have a high intrinsic structural propensity to self-associate by beta-strand stacking (3, 4).

This two-sided nature of APRs can be exploited to inactivate protein function by misfolding and aggregation (5). We recently demonstrated that homologous APRs synthetized as peptides can interact with the target protein of interest in mammalian cells, bacteria, and viruses (6–8). These APR-derived peptides (termed Pept-ins™)[*] can bind to and trigger the aggregation of proteins containing a homologous APR. This process is similar to the so-called seeding of protein aggregation that is well studied in the field of amyloid diseases (9). The resulting aggregates consist of a tightly packed cross-beta structure that is achieved by stacking of interdigitating side chains and requires a high degree of sequence specificity (10, 11). It has been well described that those proteins containing homologous APRs can coaggregate and that preformed aggregates can seed the aggregation of monomeric proteins (12). We coined the Pept-in-mediated aggregation seeding process targeted protein aggregation (TPA) and here demonstrate its use to knockdown KRAS, a key oncogenic driver with a notorious difficult-to-drug status.

Wild-type (WT) KRAS is a small GTPase that cycles through its guanosine triphosphate (GTP)-bound active and guanosine diphosphate (GDP)-bound inactive conformation. GTP-bound activated KRAS binds to several downstream effector kinases thereby activating a plethora of signaling pathways including the RAF-MEK-ERK and PI3K/Akt cascades (13). KRAS is the most commonly mutated oncogene, which is thought to be mutated in about one-third of human tumors, with a high prevalence in a wide range of cancers and with especially high frequency in pancreatic (~88%), colorectal (~50%) and lung cancers (~32%) (14). The mutations are predominantly localized at codons 12, 13, and 61 [~81, 14, and 2%, respectively (14)] and interfere with its intrinsic GTPase activity keeping KRAS in the GTP-bound state constitutively activating downstream signaling pathways and driving oncogenesis (15). We have discovered that codon 12 mutations

Significance

Kirsten rat sarcoma virus (KRAS) remains a difficult-to-drug oncogene due to its shallow surface, lacking binding grooves for small molecule compounds. We circumvent this problem by targeting aggregation-prone sequence segments (APRs) of KRAS with synthetic amyloid peptides, termed Pept-ins, that induce KRAS misfolding and aggregation. Oncogenic mutations at positions 12 and 13 amplify the aggregation propensity of an APR. A Pept-in encoding the G12V-amplified APR induces the aggregation of KRAS in vitro and in cells. We also find that this Pept-in inhibits pAkt signaling in endogeneous G12V cancer lines and suppresses tumor growth after subcutaneous injection in a syngenic G12V mouse model. The possibility to target primary sequence segments to inactivate proteins by misfolding opens opportunities for difficult-to-drug proteins such as KRAS.

This article is a PNAS Direct Submission.

[1] To whom correspondence may be addressed. Email: joost.schymkowitz@kuleuven.be or frederic.rousseau@kuleuven.be.

This article contains supporting information online at https://www.pnas.org/lookup/suppl/doi:10.1073/pnas.2214921120/-/DCSupplemental.

---

[*] Pept-in™ is a registered trade mark of Aelin Therapeutics N.V.

increase the predicted intrinsic aggregation propensity of KRAS and explored a TPA approach to exploit this intrinsic vulnerability. Here, we report the design and characterization of aggregation-prone Pept-ins that induce the aggregation of KRAS.

Results

KRAS Has a Pronounced Intrinsic Aggregation Propensity. To investigate the intrinsic aggregation propensity of KRAS, we used the statistical thermodynamics algorithm TANGO (16) as our primary in-house tool to determine the presence of APRs in the KRAS polypeptide sequence, but the results were confirmed with independently developed algorithms (*SI Appendix*, Fig. S1 *A* and *B*). All APRs together constitute the intrinsic aggregation propensity of the protein (17); the actual aggregation of the protein propensity further depends on the structural context of the APRs in the natively folded protein, as well as its thermodynamic and kinetic stability. The KRAS structure consists of a globular G-domain and a flexible C-terminal hypervariable region (18). WT KRAS contains four APRs: two APRs in the N-terminal part of the G-domain before the functionally important switch I region, one central APR flanking the related switch II region and a fourth APR close to the C-terminal hypervariable region (Fig. 1 *A* and *D*). Note that the segment from residue 111 to 115 did not meet the criteria to be considered an APR (*Materials and Methods*). KRAS is the most commonly mutated RAS isoform and is predominantly mutated at codon 12 and codon 13 with G12D, G12V, G12C, and G13D comprising 70% of all KRAS mutations (Fig. 1*C*) (18). In WT KRAS, glycine 12 directly flanks the first APR (sequence: $_{6}$LVVVGA$_{11}$) and common G12 and G13 mutations significantly increase the overall aggregation score and G12V even elongates the APR in case of mutating to the hydrophobic residue valine (Fig. 1 *A* and *B*). To evaluate the intrinsic aggregation propensity of the APR region of KRAS, we obtained synthetic peptides corresponding to this segment (Res. 1 to 16) for WT and mutant. As a soluble control peptide, we mutated valine$_8$ and valine$_9$ in the WT APR to aggregation breaking residues proline and aspartic acid (Peptide WT_PD). We dissolved the peptides and incubated them for 7 d at 37 °C to allow the aggregation reaction to complete and measured the endpoint peptide solution (Fig. 1*G*). This showed a higher aggregation propensity of the G12V and G12C mutants, compared with WT and the other mutants.

We used the empirical force field FoldX (19) to investigate the effect of the mutations on the folding free energy (ΔG, kcal/mol) of the native state, as well as on the contribution of the aggregation prone regions to the stability of the native state ($\Delta G_{\mathrm{Contrib}}$). As hydrophobic regions, APRs are typically buried in the hydrophobic core and have a stabilizing effect on the folding free energy (negative values of $\Delta G_{\mathrm{Contrib}}$). The position of all APRs in WT and mutant KRAS are summarized in a so-callled stretch plot (20–22) (Fig. 1*E*), which shows the intrinsic aggregation propensity of each APR, as well as its contribution to protein stability. We have previously shown that regions in the top right-hand corner, like APR1, are most likely to engage in aggregate interactions under native conditions, since the are in the least stable regions of the protein and have the highest propensity to aggregate (20–22). On the other hand, in conditions where the unfolded state occurs, such as during translation, all APRs may, at least transiently, be available for interaction.

The effect of mutation on the aggregation propensity of a protein can be shown as a so-called mutant aggregation and stability spectrum (MASS) plot (Fig. 1*F*) (20–22). Assuming a typical error for FoldX calculations in the order of 0.5 kcal/mol, most KRAS mutations are not predicted to have a significant impact on the global thermodynamic stability of the folded KRAS protein, nor on the local stability of the APRs (Fig. 1 *E* and *J*). The exception is the destabilization of the protein by the G13D mutation. These findings are in concordance with the fact that KRAS mutations impose their oncogenic properties by interfering with GTP hydrolysis, thereby keeping the protein in a constitutively activated state (23) (in contrast to a loss of function that would result from severe destabilization). FoldX calculations on KRAS structures bound to GTP or GDP yielded similar results indicating that ligand binding does not affect structural stability predictions (Fig. 1*F*). When looking at the positions of the APRs in the KRAS structure, we see that APR2-4 are completely buried, and APR1 is most accessible in the native fold (Fig. 1*D* and *SI Appendix*, Fig. S1*C*).

We recombinantly purified KRAS variants G12C, G12V, G12D, and G13D (residues 1 to 179) from overexpression in *Escherichia coli* BL21 based on a previously described protocol (24) and prepared samples at a concentration of 1 mg/mL in Tris buffer (20 mM Tris, 150 mM NaCl, 5 mM $MgCl_2$, 10% glycerol, pH 7.8). To characterize the stability and aggregation of these KRAS variants, we determined their melting (T_m) and aggregation (T_{agg}) temperatures by simultaneously measuring the intrinsic fluorescence of tyrosine and tryptophan residues and the static light scattering (SLS) at 266 nm during a thermal unfolding ramp from 15 °C to 95 °C with a rate of 0.3 °C/min (Fig. 1*H* and *SI Appendix*, Fig. S2*A*). For a more detailed description regarding the T_m and T_{agg} calculations see *Materials and Methods*. Of note, all variants were verified to be monomeric at the onset using size-exclusion chromatography, followed by multiple angle light scattering (SEC-MALS) (*SI Appendix*, Fig. S1*D*). Both WT and mutant KRAS appeared to possess high thermal stability, showing melting temperatures above 60 °C, with all mutants showing an increase in T_m, except for G13D, which showed a reduced T_m, in accordance with the FoldX analysis. When comparing T_m to T_{agg}, it is important to bear in mind that since the vast majority of proteins harbor several APRs, most proteins aggregate at the latest when the melting temperature is reached and the protein unfolds, exposing all its APRs (20). However, all KRAS variants analyzed here have in common with the WT an aggregation onset temperature that occurs more than 15 °C before the melting temperature (Fig. 1 *I* and *J*), i.e., well before the main unfolding transition. Moreover, the variation in T_{agg} as a result of mutation is lower than the effect on T_m. These experiments were repeated at slower and faster temperature ramp rates (0.1 and 1 °C/min, respectively) to account for kinetic effects (*SI Appendix*, Fig. S2 *B* and *C*). This showed that although the apparent Tm increases with the scan rate, the T_{agg} is much less dependent on this experimental parameter, so that the difference between T_{agg} and T_m increases with the scan rate. Overall, we also observe that T_{agg} and T_m correlate across mutations and conditions, suggesting that both processes are connected (correlation = 0.83, *P* value = 0.005). To confirm the aggregation propensity of WT and mutant KRAS, we also performed an isothermal aggregation assay using SLS at 25 °C (*SI Appendix*, Fig. S2*D*), which indeed showed aggregation over time for WT KRAS, which was more pronounced for the mutants. Together, these data show that KRAS aggregates from near-native conformations, making it an excellent candidate for TPA (20). Importantly, similar near-native aggregation propensity has been proposed in the past for antibodies (20) and membrane proteins (25), particularly in high concentrations (26). Aggregation of native states was also recently highlighted as a common feature that promotes oligomerization of soluble enzymes (27, 28). Studies have shown that minimal local unfolding of soluble proteins is enough to promote this, for instance due to thermal

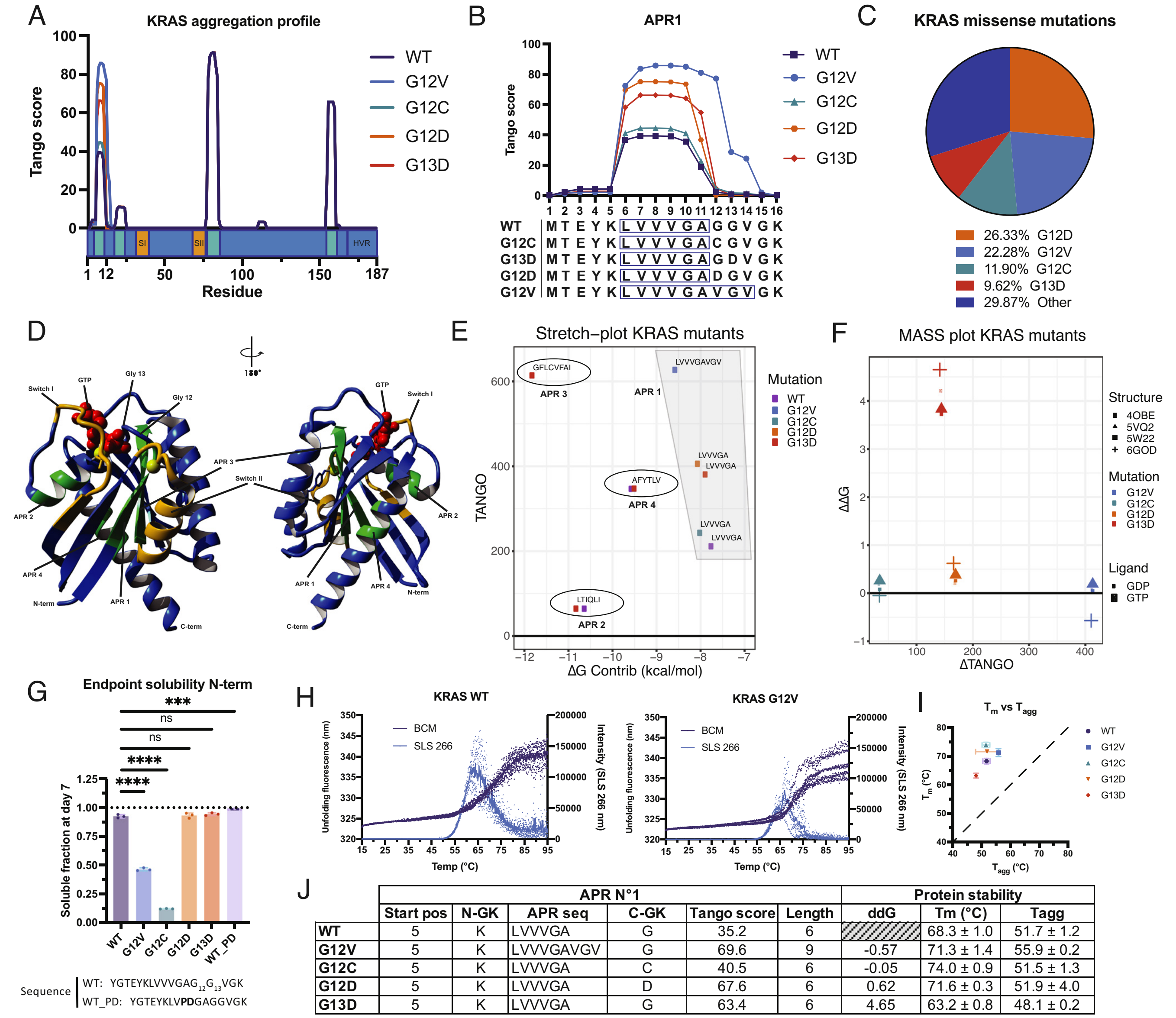

	APR N°1						Protein stability		
	Start pos	N-GK	APR seq	C-GK	Tango score	Length	ddG	Tm (°C)	Tagg
WT	5	K	LVVVGA	G	35.2	6	▨	68.3 ± 1.0	51.7 ± 1.2
G12V	5	K	LVVVGAVGV	G	69.6	9	-0.57	71.3 ± 1.4	55.9 ± 0.2
G12C	5	K	LVVVGA	C	40.5	6	-0.05	74.0 ± 0.9	51.5 ± 1.3
G12D	5	K	LVVVGA	D	67.6	6	0.62	71.6 ± 0.3	51.9 ± 4.0
G13D	5	K	LVVVGA	G	63.4	6	4.65	63.2 ± 0.8	48.1 ± 0.2

Fig. 1. Aggregation tendency and intrinsic stability of KRAS WT and mutants. (*A*) Predicted aggregation tendency shown as TANGO score per residue of KRAS4b WT (Uniprot P01116-2) and mutants. (*B*) Zoom on TANGO predicted aggregation tendency of APR1. (*C*) KRAS missense mutational spectrum from The Cancer Genome Atlas (TCGA) (n = 790, Data release 21.0). (*D*) Structure of KRAS displaying the APRs (green) and Switch I & II regions (yellow). PDB 6GOD (KRAS full length WT GPPNHP). (*E*) Stretch-plot showing aggregation propensity (TANGO) and free energy contribution ($\Delta G_{\mathrm{Contrib}}$) of each APR in WT and mutant KRAS. (*F*) Mutant Aggregation and Stability Spectrum (MASS) plot displaying changes in free energy ($\Delta\Delta G$) and aggregation propensity (ΔTANGO) between WT and different KRAS mutants for GTP- (PDBs 6GOD and 5VQ2) and GDP-bound structures (PDBs 4OBE and 5W22). (*G*) Solubility after 7 d at 37 °C in Dulbecco's phosphate-buffered saline (DPBS) of peptides covering the N-terminal region (res. 1 to 16) of KRAS WT and mutants. Peptide WT_PD has two aggregation-breaking mutations (Pro and Asp) in the WT sequence. Soluble fraction after 7 d normalized to freshly dissolved at day 1. n = 3, mean ± SD, one-way ANOVA with Dunnett's multiple comparisons test. ns, not significant, ****P* < 0.001, *****P* < 0.0001. (*H*–*J*) Protein stability of KRAS WT and G12V. Concentration is 1 mg/mL in Tris buffer (20 mM Tris, pH 7.8, 150 mM NaCl, 5 mM $MgCl_2$, 10% glycerol). Ramp rate 0.3 °C/min. (*H*) Unfolding fluorescence as barycentric mean and static light scattering at 266 nm for KRAS WT and G12V. Representative plots from one protein batch with six replicates. See *SI Appendix*, Fig. S2A for other mutants. (*I*) Melting vs. aggregation temperature for KRAS WT and mutants. (*J*) Detailed overview of TANGO predicted aggregation propensity of APR1 of WT and mutant KRAS and measured protein stability of purified KRAS protein. mean ± SD from measurements of two independent protein productions with at least four replicates per batch.

fluctuations that occur under native conditions (3) or due to PTMs (29). An alternative that fits our derived data, however, has proposed that highly flexible exposed APRs can also promote intermolecular interactions that support native-like aggregation (30), which further supports the notion of targeting APR1 that is more exposed in the native KRAS fold.

Synthetic Peptides Derived from KRAS APRs Form Amyloids Over Time. Next, we designed synthetic peptides (Pept-ins) derived from APR1 of the G12V mutant and one peptide derived from APR3 (Fig. 2*A*), using a previously developed paradigm. Briefly, the APR-derived sequences are supercharged with flanking lysine residues and placed in tandem, separated by a glycine-serine linker (*SI Appendix*, Fig. S3*A*). While the tandem design creates a minimal seed for aggregation, the charged residues provide kinetic control of the process. Keeping in mind that the efficiency of peptide synthesis drops markedly after 20 amino acids, especially for hydrophobic and aggregation prone peptides, this imposes a length limitation on the APR of seven amino acids. For APRs that are longer, like APR1 in KRAS G12V, we employ a systematic sliding window with stepsize 1, generating a Pept-in for each subwindow of 7 (*SI Appendix*, Fig. S3*A*). As a result, each peptide in the series differs

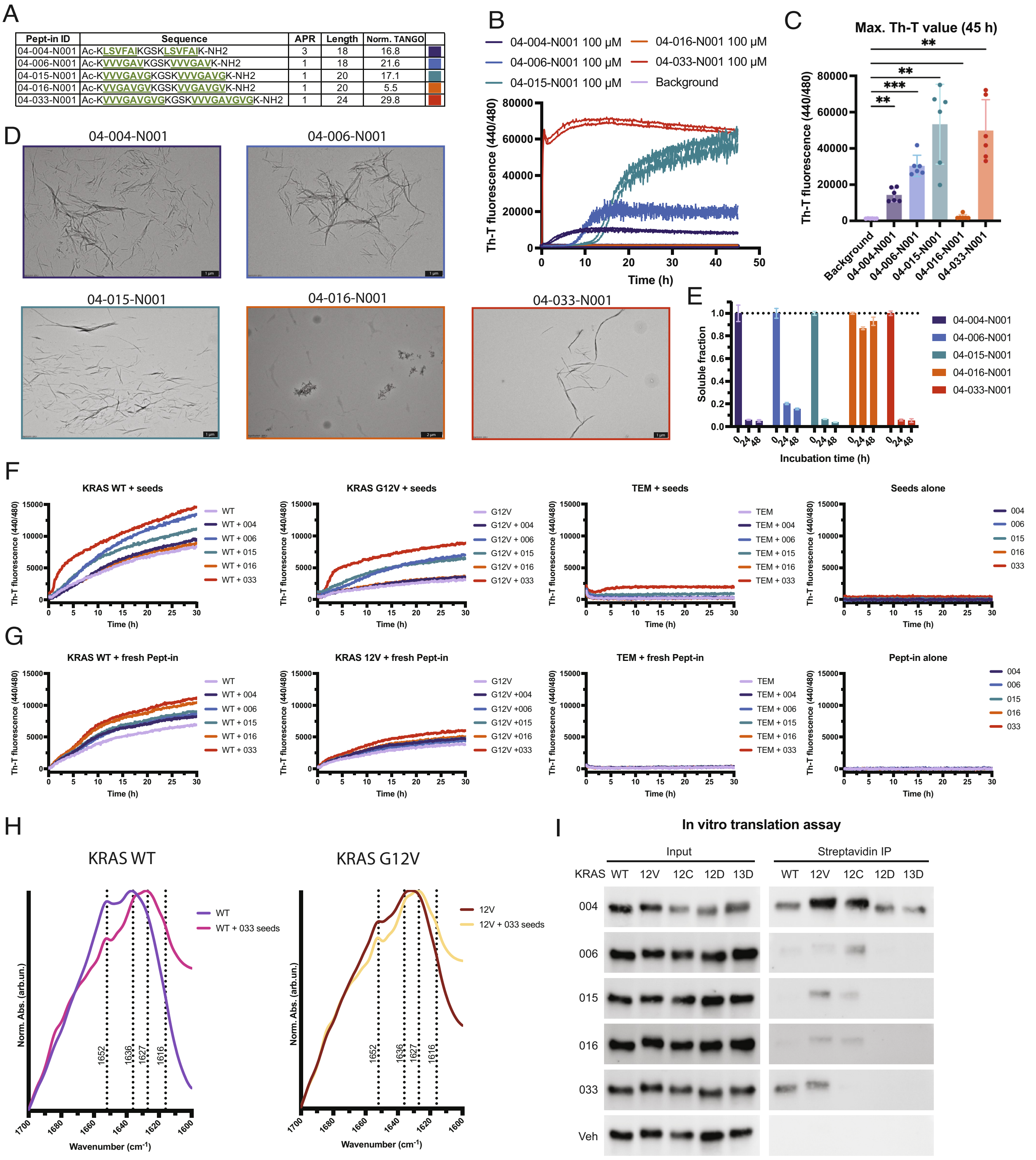

Pept-in ID	Sequence	APR	Length	Norm. TANGO	
04-004-N001	Ac-K<u>LSVFAI</u>KGSK<u>LSVFAI</u>K-NH2	3	18	16.8	■
04-006-N001	Ac-K<u>VVVGAV</u>KGSK<u>VVVGAV</u>K-NH2	1	18	21.6	■
04-015-N001	Ac-K<u>VVVGAVG</u>KGSK<u>VVVGAVG</u>K-NH2	1	20	17.1	■
04-016-N001	Ac-K<u>VVGAVGV</u>KGSK<u>VVGAVGV</u>K-NH2	1	20	5.5	■
04-033-N001	Ac-K<u>VVVGAVGVG</u>KGSK<u>VVVGAVGVG</u>K-NH2	1	24	29.8	■

Fig. 2. Design and characterization of Pept-ins derived from KRAS APRs. (*A*) Overview of Pept-ins derived from KRAS APRs. The normalized TANGO score is the total TANGO devided by peptide length. Pept-ins are given a color to ease comparison in following graphs. (*B*) Pept-in aggregation over time monitored using the amyloid-binding dye Th-T (Ex 440/Em 480, readout every 5 min). Pept-in concentration is 100 μM final concentration in DPBS. Representative plot showing two repeats per Pept-in. (*C*) Maximum Th-T values per Pept-in from (*B*). n = 6 from three independent experiments, mean ± SD, Repeated measures (RM) one-way ANOVA with Dunnett's multiple comparison test. ns, not significant, $^{**}P < 0.01^{***}P < 0.001$. (*D*) TEM images of samples after 24-h incubation at 100 μM in DPBS. (*E*) Pept-in solubility measured after 24-h and 48-h incubation at 37 °C in DPBS. n = 3, mean ± SEM. (*F*) Th-T fluorescence over time of KRAS WT and G12V protein mixed with Pept-in seeds from Hepes stocks (9:1 molar ratio of protein to seeds). Unrelated TEM protein mixed with and without Pept-in seeds and Pept-in seeds alone are shown as controls. n = 6 from three independent experiments. Plots show mean of one representative experiment with duplicates. (*G*) Th-T fluorescence of KRAS WT and G12V protein and TEM protein mixed with freshly dissolved Pept-in (9:1 molar ratio of protein to Pept-in). Plot shows mean of n = 3. (*H*) FTIR spectra of KRAS WT and G12V protein incubated 5 h at 37 °C with 033 seeds from Hepes stocks (1:1 molar ratio of protein and seeds). (*I*) Results of in vitro translation of KRAS WT and mutants in the presence of biotin-labeled Pept-in (10 μM) for 2 h at 37 °C followed by pull-down using streptavidin-coated beads. Input (before pull-down) and streptavidin IP fractions are shown. Results are shown from one experiment of n = 3. *SI Appendix*, Fig. S4*J* shows another independent repeat.

slightly in its physicochemical properties, including aggregation propensity. From here on Pept-ins are referred to by their full or shortened ID shown in Fig. 2*A*, (e.g. 04-**004**-N001 or Pept-in **004**). Pept-in 004 was derived from APR3, and is hence identical in all KRAS mutants, whereas Pept-ins 006, 015, 016, and 033 are based on subwindows of APR1, and are hence different between the mutants (Cfr Fig. 1*G*, showing the higher intrinsic aggregation of G12V and G12C). De novo structure prediction using PEP-FOLD3 (31) models depicts these Pept-ins as hairpin-separated beta-strands (*SI Appendix*, Fig. S3*B*). These models correspond well to the beta-aggregation prediction scores of the TANGO algorithm. Pept-ins 004, 006, 015, and 033 have normalized TANGO scores >15 and a distinct beta-hairpin-beta structure. In contrast, Pept-in 016 was predicted to be predominantly random coil and has the lowest TANGO score in the series, falling close to the treshold of 5% per residue, which was previously shown to be a good cutoff below which little or no aggregation is experimentally observed (Fig. 2*A*) (16). In agreement, Pept-ins 004 and 033 were consistently identified as the most aggregation prone by several other predictors applied, whereas Pept-in 016 was shown to be the weakest and in most cases scored below the threshold of detection (*SI Appendix*, Fig. S3 *C* and *D*).

This effect, where not all the peptins derived using the sliding window approach retain the aggregation propensity, has been observed previously (6–8), and provides us here with a control that allows differentiating between mere sequence similarity with KRAS to see our effects or the need for actual aggregation. We obtained all Pept-ins from solid-state synthesis (followed by HPLC purification), and measured their aggregation at 37 °C at pH 7.2 over time using the amyloid-binding dyes Thioflavin-T (Th-T) and penta-formylthiophene acetic acid [p-FTAA (32)] at 100 μM total peptide concentration (Fig. 2 *B* and *C* and *SI Appendix*, Fig. S4 *A* and *B*). Pept-ins 004, 006, 015, and 033 all showed dose-dependent sigmoidal Th-T binding over time (*SI Appendix*, Fig. S4 *C–G*) that is typical of amyloid-like aggregation, in line with their design. As expected from the TANGO analysis, Pept-in 016 showed minimal dye binding over time, with low maximum fluorescence intensity values (Fig. 2*C*). Imaging of start point and end point samples using Transmission Electron Microscopy (TEM) revealed typical fibrillar protein aggregates for all Pept-ins, thereby confirming the dye-binding results (Fig. 2*D* and *SI Appendix*, Fig. S5). The contrasting behavior of Pept-in 016 was further highlighted by end-point solubility analysis. Specifically, although the soluble fraction for all peptides was reduced by 80% or more after 24 h of incubation, only a small percentage of Pept-in 016 (15%) was found in the insoluble fraction within the same timeframe, thus verifying its minimal aggregation propensity (Fig. 2*E*). Circular dichroism showed a beta-sheet secondary structure as the primary component of sonicated and nonsonicated end-point samples for Pept-ins 004, 015, and 033, which is characteristic of amyloid fibers, with a stronger presence of random coil structures for Pept-ins 006 and 016, respectively (*SI Appendix*, Fig. S4 *H* and *I*). These data confirm the predicted aggregation potential of the synthetic peptides, a prerequisite for TPA (6, 8), and identify Pept-In 016 as a nonaggregating control emerging from the same series.

Seeding of Folded Protein and Cotranslational Pept-In-KRAS Interaction. A characteristic of protein aggregation is a phenomenon called "seeding", in which the rate of aggregation of monomeric protein is increased by adding preformed aggregates, typically fragmented mature fibrils of the same protein, to the monomer solution (33). This process is sequence specific, meaning that it is most efficient when the preformed aggregates are homologous to the monomeric protein (6, 34). Since TPA relies on the ability of the Pept-ins to induce the aggregation of the full-length protein, we evaluated the seeding capacity of the aggregating Pept-ins on purified KRAS protein under native conditions. Seeds were prepared for each Pept-In by fragmenting end-stage fibrils via sonication, which was verified using TEM (*SI Appendix*, Fig. S5 for TEM images of seeds, *SI Appendix*, Fig. S4*H* for CD spectra). Each seed preparation was separately mixed with monomeric KRAS protein, and incubated at 37 °C at pH 7.8, and aggregation was monitored over time using Th-T fluorescence. Seed preparations of Pept-ins 006, 015, and 033 effectively increased the aggregation of both KRAS WT and G12V, but not the unrelated control protein bacterial TEM-1 β-lactamase (Fig. 2*F*). Pept-Ins 016 and 004 did not show seeding in this assay. Also, the aggregation effect was greatly reduced when freshly dissolved Pept-ins were added (Fig. 2*G*). These observations suggest that that preformed seeds are required to induce KRAS aggregation, in line with the seeding literature (35). Addionally, we verified the seeding effect of Pept-ins seeds and freshly dissolved Pept-in on KRAS G12C, G12D, and G13D and observed increased aggregation of KRAS G12C and G12D when mixed with Pept-in seeds of 006, 015, and 033 and again reduced seeding with freshly dissolved Pept-in (*SI Appendix*, Fig. S6 *A* and *B*). KRAS G13D showed rapid baseline aggregation in accordance with previous stability analysis.

As a final confirmation of the aggregation-inducing effect of peptides 015, 016, and 033 on KRAS protein in vitro, we performed Fourier-transform infrared spectroscopy (Fig. 2*H* and *SI Appendix*, Fig. S6*C*), which allows to characterize the secondary structure content of protein samples before and after exposure to preformed Pept-in seeds (1:1 molar ratio). Seed concentration in this setup was below the detection limit (0.1 mg mL^{-1}), and therefore, spectral contributions from the seeds were negligible. Using this setup, we observed a clear shift from the alpha helical components in the spectrum derived from both the WT and the mutant KRAS and toward the formation of intermolecular beta-sheet structures, independently confirming the formation of beta-rich aggregates in the mixed samples with Pept-ins 015 and 033. The mixed samples with nonaggregating Pept-in 016 did not show this spectral shift (*SI Appendix*, Fig. S6*C*).

Further, we decided to investigate the ability of our Pept-ins to interact with KRAS in a cotranslational manner. When proteins are being translated at the ribosome, the APRs are temporarily exposed before being incorporated in the native structure by the folding process, and may hence allow access to Pept-ins. To investigate this, we set up an in vitro translation assay using biotinylated Pept-ins to assess Pept-in-KRAS interactions during translation based on the PURExpress cell-free translation system and monitored the interaction of the Pept-ins with the nascent chain via streptavidin pull-down followed by western blot (Fig. 2*I* and *SI Appendix*, Fig. S4*J*). Pept-In 004, targeting APR 3 showed interaction with all KRAS constructs in this experiment, whereas for most Pept-Ins derived from APR1, we observed preferential binding to the G12V and G12C mutants, consistent with their increased aggregation propensity (Fig. 1*G*). Given that during the timeframe of this experiment no Th-T signal is observed (*SI Appendix*, Fig. S4 *A–G*) and that the nonaggregating Pept-in 016 also showed this binding pattern, these data suggest that the initial interaction between KRAS nascent chain and Pept-in does not require preformed seeds, although the formation of soluble oligomeric species that fall below our detection limit cannot be excluded.

Pept-In Interactions with KRAS in Cells. Next, we explored whether Pept-in-KRAS interactions could also be observed in a cellular context. First, KRAS engagement was explored in RAS-less mouse embryonic fibroblasts (MEFs), that were obtained from the RAS initiative (National Cancer Institute, USA). These cell lines have been generated and extensively characterized by Drosten et al. (36). In short, these are MEFs where endogenous N-, H-, and KRAS genes are removed and subsequently transduced with a specific KRAS gene (WT or a specific mutant). As a result, the MEF cell line is dependent on the expression of the transgene for continuous proliferation, and the isogenic background allows the evaluation of specificity. Overnight treatment with monomeric biotinylated Pept-in followed by streptavidin pull-down from the cell lysates, and western blot showed binding of both KRAS G12V and WT for the aggregating Pept-ins 006, 015, and 033 and only some WT binding for 004 (*SI Appendix*, Fig. S7*A* and quantification in *SI Appendix*, Fig. S7*B*). No interaction was observed for the nonaggregating Pept-in 016 and the vehicle control.

Next, we turned to cancer cell lines carrying an endogenous KRAS G12V mutation (heterozygous), starting with NCI-H441 cells (lung adenocarcinoma). Flow cytometry analysis of cells treated with fluorescein isothiocyanate (FITC)-labeled Pept-ins confirmed earlier observations that Pept-ins with this design are taken up into cells (6, 8, 37). The data showed that peptides 004, 006, 015, and 033 showed 80 to almost 100% cell uptake in 3 h, whereas 016 showed 30% (*SI Appendix*, Fig. S8 *A* and *B*). As previously observed this is related to their aggregation property, as the nonaggregating control 016 showed only 30% positive cells at the same time point. We then treated the cells 16 h with biotinylated derivatives of the Pept-ins and performed a streptavidin pull-down of the Pept-in, followed by detection of the associated KRAS pulled from these cells. This experiment showed that interactions formed between the Pept-ins and endogenous KRAS in these cells (Fig. 3*A* and quantification in Fig. 3*B*), in a similar fashion as was observed in vitro. Next, we treated NCI-H441 cells with unlabeled Pept-ins for 24 h, followed by fractionation of the lysate into a soluble and insoluble fraction. Pept-in treatment with all aggregating Pept-in variants resulted in an enrichment of KRAS in the insoluble fraction suggesting that part of the cellular KRAS pool is converted to aggregates (Fig. 3*C* and quantification in *SI Appendix*, Fig. S7*C*). We checked if this enrichment of insoluble KRAS was accompanied by an enrichment of heat shock protein 70, a chaperone that is known to bind to protein aggregates (38), but we did not detect an enrichment of HSP70 in the pellet fraction (Fig. 3*C* and quantification in *SI Appendix*, Fig. S7*C*). Subsequently, we detected a mild increase in cleaved PARP in these cells treated with 004, 006, and 033, which suggests that Pept-in treatment results in apoptotic cell death (39). This is in line with previous reports linking KRAS degradation or inhibition with PARP cleavage (40, 41). To confirm the link to apoptosis, we also performed the Apo-ONE Caspase-3/7 assay (Promega), which is based on a quenched fluorescent caspase-3/7 consensus substrate peptide. Upon caspase activation, this peptide is cleaved, resulting in a fluorescence increase. These results (Fig. 3*D*) confirm the PARP cleavage data and show induction of apoptosis by Pept-ins 006, 015, and 033 in the NCI-H441 cells. Next, we also assesed the effects of Pept-ins on endogenous WT KRAS. For this, we focussed on the lung adenocarcinoma cell line NCI-H1299. This cell line showed excellent uptake (>90%) of all FITC-labeled Pept-ins after 3 h (*SI Appendix*, Figs. S8*B* and S9*A*). Treatment of unlabeled Pept-ins followed by lysate fractionation did not result in an enrichment of KRAS or HSP70 in the insoluble fraction or PARP cleavage (undetectable) (Fig. 3*E*, quantifications in *SI Appendix*, Fig. S7*D*). Pept-in treatment resulted only showed some Caspase-3/7 activition for 015 (*SI Appendix*, Fig. S7*G*).

However, since the main goal of the Pept-ins is to functionally inactivate KRAS in cancer cells, we decided to use a signaling assay to select Pept-ins for further studies. Mutant KRAS exerts its oncogenic properties via multiple downstream signaling pathways including the RAF-MEK-ERK and PI3K-AKT pathways (illustrated in *SI Appendix*, Fig. S7*E*) (42). A previous study by Tang et al. showed that ERK1/2 phosphorylation can be increased as a result of proteotoxic stress (43), confounding the inhibitory effect from KRAS inhibition. In this light, we examined the levels of phosphorylated ERK1/2 (p-ERK1/2, Thr202/Tyr204) and AKT (p-AKT, S473) in NCI-H441 cells upon treatment with KRAS siRNA and selected Pept-ins and observed a stronger inhibition of p-AKT than p-ERK1/2 (Fig. 3*F*, quantifications in *SI Appendix*, Fig. S7*F*). In order to better quantify the effect of Pept-in treatment on p-AKT and total AKT, we moved to the MSD multiarray sandwich immunoassay coupled to electrochemiluminescence for readout (Mesoscale Diagnostics). We compared the activity of all Pept-ins at multiple concentrations in NCI-H441 cells and observed a significant reduction in p-AKT/total AKT levels compared with vehicle control after 24-h treatment with 10 μM, except for the nonaggregating 016 (Fig. 3*G*). These levels of p-AKT inhibition were comparable with those achieved with KRAS siRNA transfection in this cell line. Dose–response analysis of Pept-in 015 in NCI-H441 cells showed maximum p-AKT inhibition of 54 % after 24 h (Fig. 3*G*). Pept-in 033 resulted in 45% reduction after 24 h in the same cells. The dose–response curves of the other peptides indeed were less compelling (Fig. 3*G*).

We then extended the analysis to a small panel of additional cell lines: namely colorectal adenocarcinoma SW620 (homozygous for KRAS G12V), as well as the previously used NCI-H1299 (KRAS WT) and Hela cells (KRAS WT). We checked p-AKT/total AKT levels compared with vehicle control in these cell lines after 24-h treatment with 10 μM. This showed that the effect of Pept-ins 006, 015, and 033 translated to the SW620 lines, but although a limited reduction in signal was observed in the WT lines, this was not statistically significant (Fig. 3*H*). Some activition of Caspase-3/7 could be detected in the SW620 and HeLa cells upon treatment (*SI Appendix*, Fig. S7*G*).

Since uptake efficiency can vary between cells, we performed flow cytometry analysis of cellular uptake using fluorescently labeled Pept-ins as before and found similar or higher uptake efficiencies in these lines, compared with the NCI-H441 cells, suggesting that these experiments are not limited by the peptide uptake (*SI Appendix*, Figs. S8*B* and S9 *A*–*C*). Based on these data we selected Pept-ins 015 and 033 as the most promising candidate hits from our KRAS series, and the low aggregating peptide 016 as a negative control.

Visualization of KRAS Aggregation in Cells. Next, we aimed to visualize the interaction between Pept-ins and KRAS in a cellular context. In concordance with a previous report from Waters et al. (44), we noticed that currently available RAS antibodies are not suitable for immunofluorescence. To solve this issue, we created two reporter cell lines (HeLa), expressing an mCherry-KRAS fusion for WT and G12V, respectively, and taking a cell line expressing mCherry along as a basic control. As expected, fusion of mCherry to KRAS induced a shift of its intracellular location from diffuse cytoplasmic (free mCherry) to the cell membrane (KRAS-mCherry, *SI Appendix*, Fig. S10*A*), but the fusion also resulted in a significant accumulation of KRAS inclusions, consistent with the aggregation of the fusion construct. Moreover, this effect that was more pronounced in the WT fusion than the G12V, making it harder to directly compare both lines in terms of induced aggregation (*SI Appendix*, Fig. S11*F*).

First, we did a treatment of the KRAS reporter lines with a FITC-labeled version of Pept-in 015, 016, and 033 and studied

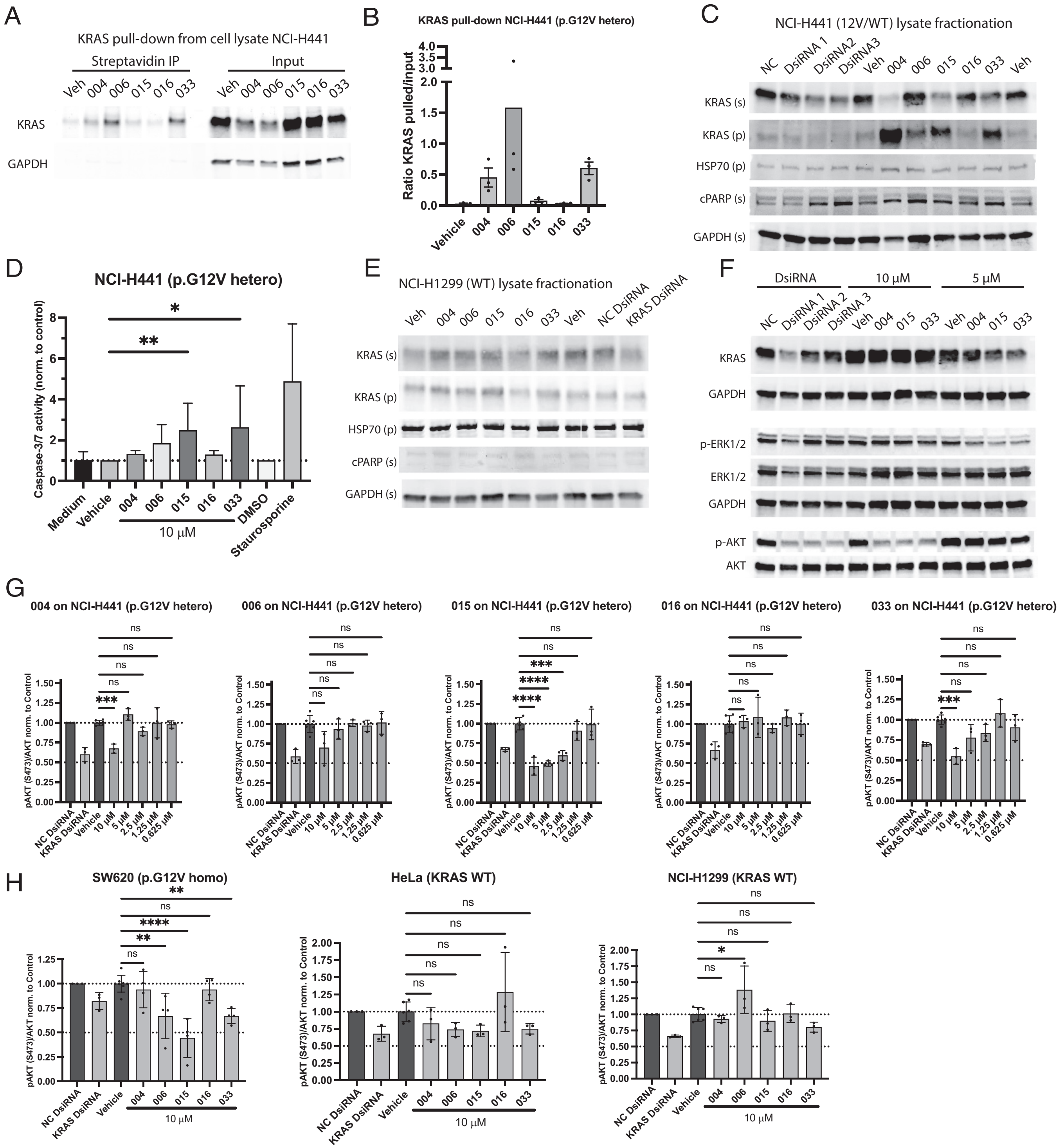

Fig. 3. KRAS-Pept-in target engagement and cellular effects. (*A*) Streptavidin pull-down and detection of KRAS protein in lysate of NCI-H441 cells. Cells were treated 16 h with 25 μM biotinylated Pept-in versions or vehicle. Input represents lysate fraction before pull-down. (*B*) Quantification of KRAS pull-downs in (*A*). Ratio of KRAS signal detected in streptavidin IP over input. n = 3, mean ± SD. (*C*) KRAS protein levels in soluble (s) and pellet (p) lysate fraction of NCI-H441 treated with 10 μM Pept-in or vehicle for 24 h. HSP70 detected in pellet. Cleaved PARP and housekeeping GAPDH detected in soluble lysate fraction. DsiRNA controls represent cells transfected with 10 nM DsiRNA NC control and three KRAS targeting DsiRNAs at timepoint 0. Quantifications of blots in *SI Appendix*, Fig. S7*C*. (*D*) Caspase-3/7 activity in NCI-H441 cells after 24-h treatment with 10 μM Pept-ins or vehicle. 500 nM staurosporine was included as assay control. Signal normalized to respective controls; vehicle for Pept-ins, DMSO for Staurosporine. n = 5, mean ± SD, Kruskal–Wallis with Dunn's multiple comparison test to test Pept-in normalized to vehicle. *$P < 0.05$, **$P < 0.01$. (*E*) KRAS protein levels in soluble (s) and pellet (p) lysate fraction of NCI-H1299 treated with 10 μM Pept-in or vehicle for 24 h. HSP70 detected in pellet. Cleaved PARP and housekeeping GAPDH detected in soluble lysate fraction. DsiRNA controls represent cells transfected with DsiRNA (15 nM NC control and mix of three KRAS targeting, 5 nM each) at timepoint 0. Quantifications of blots in *SI Appendix*, Fig. S7*D*. (*F*) KRAS, GAPDH, p-ERK1/2 (Thr202/Tyr204), total ERK1/2, p-AKT (S473) and total AKT protein levels in lysates of NCI-H441 treated with indicated concentrations of Pept-in for 24 h. DsiRNA controls are the same as in (*C*). Quantifications of blots in *SI Appendix*, Fig. S7*F*. (*G*) MSD immunoassay quantification of p-AKT (S473) inhibition in NCI-H441 after 24-h treatment with Pept-in or DsiRNA, same as (*E*). Dose–responses of all Pept-ins. n = 3, mean ± SD, one-way ANOVA with Dunnett's multiple comparison test. ns, not significant, ***$P < 0.001$, ****$P < 0.0001$. (*H*) MSD assay on SW620, HeLa and NCI-H1299 cells after 24-h treatment with 10 μM. n ≥ 3, mean ± SD, one-way ANOVA with Dunnett's multiple comparison test. ns not significant, *$P < 0.05$, **$P < 0.01$, ****$P < 0.0001$.

the effect after a short period of incubation (2 h). This resulted in Pept-in uptake and induction of perinuclear inclusions in a dose-dependent manner for Pept-ins 015 and 033, but not 016 in both KRAS and free mCherry cells (*SI Appendix*, Figs. S10 *B–D* and S11 *D* and *E*). Such perinuclear inclusion bodies are the typical subcellular compartments where aggregates of misfolded proteins are found. At the highest magnification of our instrument, we observed apparent overlap between FITC (Pept-in) and mCherry (KRAS) spots at 10 µM treatment with 015 and already at 2.5 µM treatment with 033 in both the KRAS WT and the KRAS G12V cell lines (*SI Appendix*, Fig. S10 *B* and *C*), but not the free mCherry cell line (*SI Appendix*, Fig. S10*D*). Next, we setup a high-content screening method using 40x magnification images (*SI Appendix*, Fig. S11 *A–C*) to study the colocalization between Pept-in and protein spots. No protein spots could be detected and quantified in the cell expressing free mCherry (*SI Appendix*, Fig. S11 *A–C, F,* and *G*). Therefore, we focussed on the KRAS WT and G12V cells to quantify colocalization and found a significant overlap of Pept-in on protein spots that was higher for G12V than for WT KRAS (*SI Appendix*, Fig. S11 *H* and *I*). However, at this early time point, there is a dose-dependent difference between the Pept-ins: 015 shows only strong overlap at the highest concentration, whereas 033 shows an effect already at the lowest concentration (*SI Appendix*, Fig. S11 *H* and *I*). When we quantified the effect of Pept-in on KRAS aggregation (number of protein spots) in this setup, we observed robust increase in KRAS aggregation only with 033 and the G12V KRAS construct, although 033 did show a modest effect on WT (*SI Appendix*, Fig. S11 *J–M*). Pept-in 015 did not show increased aggregation at this time point, possibly because of its slower aggregation kinetics.

Second, we also investigated the effect of treatment with unlabeled Pept-in in the form of seeds as were used in the in vitro seeding assays on recombinantly produced KRAS (Fig. 2*F*), produced by sonicating mature aggregates, a process that is very widely adopted in the field. Although we observed a similar induction of perinuclear inclusion bodies (*SI Appendix*, Fig. S12 *A–D*) as with the freshly dissolved peptides, the effect of the Pept-ins was reversed: In this configuration, 015 generated robust increase in aggregation of mainly KRAS G12V and to a lesser extent, WT (*SI Appendix*, Fig. S12 *B–E*). The seeds of 033 peptide, on the other hand, showed only a modest effect. We were not able to fully rationalize these differences, but it is well known that the efficiency of seed generation by sonication differs between peptides.

As an additional control, we turned to extensively studied aggregation sensor lines, namely for the yeast prion protein Sup35 and the human Tau protein (involved in Alzheimer's disease and other tauopathies). We employed previously established mammalian biosensor cell lines for Tau and Sup35, respectively expressing cyan- and yellow fluorescent protein (CFP/YFP)-labeled Tau in Hek293 cells (45) or green fluorescent protein (GFP)-labeled Sup35NM domain in N2A cells (46). These lines show little or no background aggregation and, as described, these cell lines selectively show induced aggregation upon transfection of amyloid seeds of recombinantly prepared Tau or Sup35NM to these cells, respectively. Transfection or simple addition of KRAS-targeting Pept-in seeds did not show any induced aggregation in these biosensor cell lines (*SI Appendix*, Fig. S13 *A* and *B*), and vice versa, addition of Tau or Sup35NM seeds to the KRAS biosensor did not induce KRAS aggregation (*SI Appendix*, Fig. S12 *A–C*). Together these results confirm an intracellular Pept-in-KRAS interaction and the induced aggregation of target protein.

The Effect of KRAS Pept-Ins on Cancer Cells. To evaluate the potential of induced KRAS aggregation as a possible therapeutic avenue, we tested the effect of Pept-in treatment on cell viability across a panel of cancer cell lines with different KRAS genotypes: KRAS$^{\text{WT/WT}}$ Kras (NCI-H1299 and HeLa), KRAS$^{\text{G12C/WT}}$ (NCI-H358), KRAS$^{\text{G12C/G12C}}$ (Mia PaCa-2), KRAS$^{\text{G12D/WT}}$ (PANC-1), KRAS$^{\text{G12V/WT}}$ (NCI-H441, NCI-H727), KRAS$^{\text{G12V/G12V}}$ (Capan-1, LCLC-97TM1, SW-620), and KRAS$^{\text{G13D/WT}}$ (HCT-116). Each cell line was cultured in a 3D model, treated with different doses of Pept-Ins 004, 006, 015, 016, and 033, and cell viability was monitored to determine the 50% inhibitory concentration (IC$_{50}$). No effect on viability could be observed in any of the tested cell lines for the nonaggregating Pept-in 016 (*SI Appendix*, Fig. S14*A*). Dose-dependent inhibition of cell viability could be observed across cell lines with best responders being affected in the low micromolar concentration range (Fig. 4*A*). Cell lines carrying heterozygous G12V (NCI-H441 & NCI-H727) or G12C (NCI-H358 & Mia PaCa-2) mutations were among the best responders to our Pept-in treatments, with Pept-in 033 showing the lower IC$_{50}$ values. However, WT lines (in particular HeLa), also showed loss of viability. To determine to what extent these effects could stem from unspecific aggregate-mediated toxicity, we determined the IC$_{50}$ of our Pept-ins on peripheral blood mononuclear cells (PBMCs) and generally observed mild toxicity at higher doses for Pept-ins 006, 015 and 033. More severe cytotoxicity could be observed at the two highest doses for Pept-in 004 (Fig. 4*B* and *SI Appendix*, Fig. S14*B*). The nonaggregating Pept-in 016 did show any effect on PBMC viability.

Finally, we performed an in vivo study in a KRAS-driven preclinical murine lung cancer model (Fig. 4*C*). Kras$^{+/\text{LSLG12V}}$;Trp53$^{\text{L/L}}$ mice were infected with low-titer Adeno-Cre virus particles by intra-nasal instillation to allow expression of Kras$^{\text{G12V}}$ and deletion of Trp53. Deletion of Trp53 in KRAS mutant mice induces spontaneous generation of advanced lung adenocarcinoma with close resemblance to its human counterpart (47). Endpoint tumors were harvested and tumor pieces were implanted subcutaneously in the left dorsal flank of syngeneic and fully immunocompetent mice. For clarity, Fig. 4*C* further illustrates the setup of this mouse model. We selected Pept-in 033 for all in vivo experiments based on all the in vitro data. Tumor growth was monitored in control and Pept-in (04-033-N001)-treated mice cohorts during 24 d (of which 21 d of daily subcutaneous treatment, as before). Mean animal weights of all study groups continuously increased during the study (*SI Appendix*, Fig. S14*C*), confirming the absence of major adverse events. As measured on Day 21, untreated and vehicle groups showed exponential increase in tumor size (Fig. 4 *D* and *E*). Vehicle treatment did not show noticeable tumor inhibition compared with the untreated group, whereas treatment with the clinically approved MEK inhibitor Trametinib and the KRAS-targeting Pept-in 04-033-N001 resulted in significant inhibition of primary tumor growth compared with vehicle (Adjusted $P = 0.0381$ and 0.0356 respectively, ANOVA post hoc Dunnett's) (Fig. 4*E*).

Three mice in both the untreated and vehicle groups were euthanized earlier because tumor sizes exceeded ethically acceptable limits (Fig. 4 *F* and *G*). In addition, one animal in both untreated and vehicle groups and two animals in the Trametinib group were euthanized before end point because of tumor ulceration. Importantly, no ulceration or ethical excess of tumor size was observed in the 04-033-N001 treated group (Fig. 4 *G–I*). In summary, we demonstrated significant antitumor efficacy without adverse effects of one Pept-in in a KRAS-driven mouse allograft tumor model.

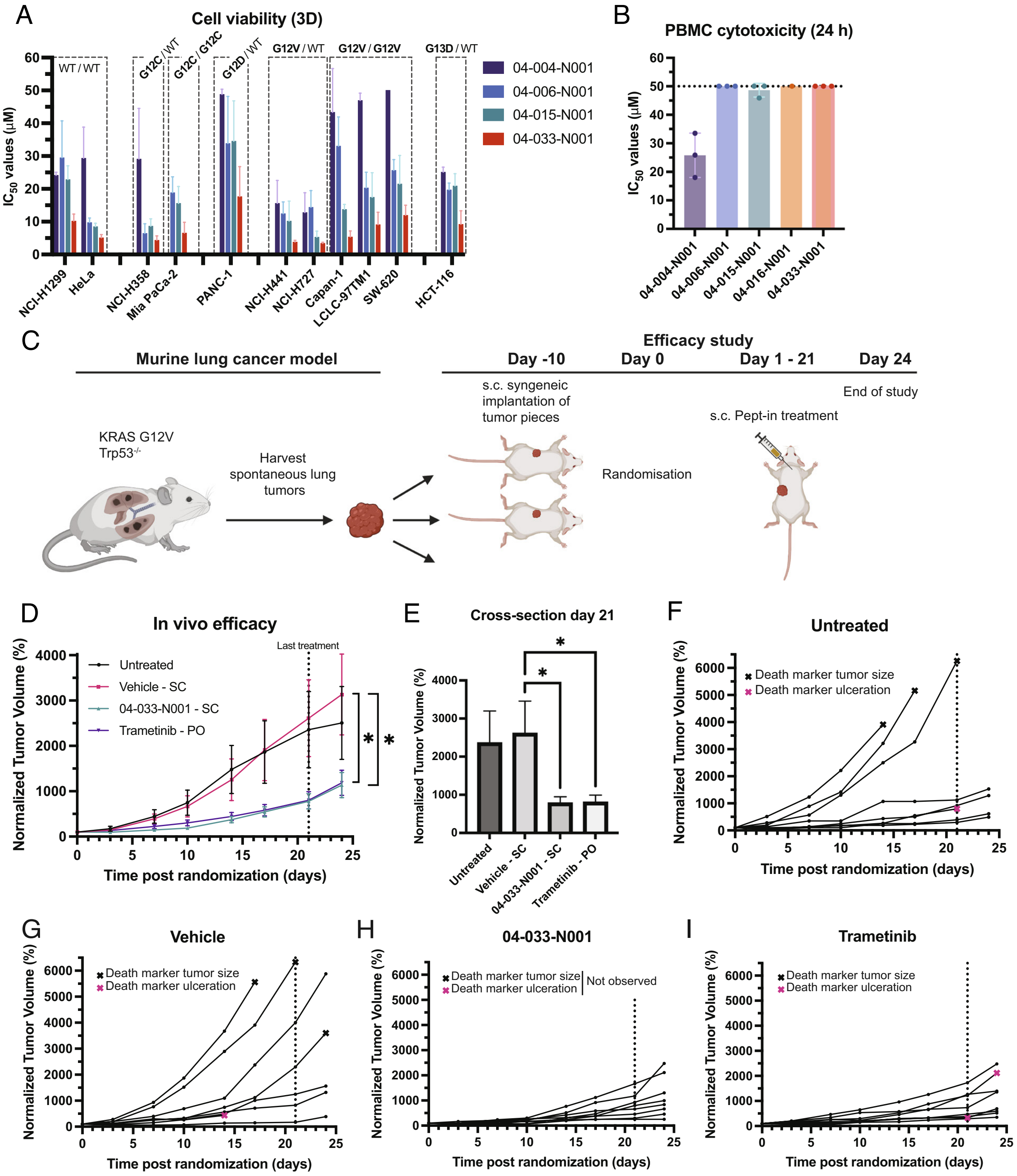

Fig. 4. Anticancer activity of Pept-ins. (*A*) IC$_{50}$ values of cancer cell line viability in 3D assay. Cell viability read-out after 5 d. Data represent mean ± SD from at least two independent experiments with two technical replicates per condition. (*B*) Cytotoxicity assay on peripheral blood mononuclear cells after 24-h treatment. Data from three independent experiments with two technical replicates, except Pept-in 016 (1 experiment with 2 replicates). (*C*) Illustration of mouse model and efficacy study. Created with BioRender.com. (*D*) Mice with subcutaneous KRAS-driven tumor received daily subcutaneous injections for 21 d of 20 mg/kg Pept-in or vehicle. Positive control cohort received daily 3 mg/kg Trametinib via oral administration. One group received no treatment. Tumor volumes were measured every 3 or 4 d. Each treatment group contains eight animals. Mice were killed when ethical abortion criteria were met during the study. Last observations were carried forward in case an individual was killed before end of study. Tumor volumes are normalized to day 0 (100%). Data represent mean ± SEM. Statistics represent a longitudinal analysis (mixed linear model) using type II ANOVA and pairwise comparisons with Bonferroni correction, $*P < 0.05$. (*E*) Cross-sectional analysis of normalized tumor size at last treatment day 21. Last observations were carried forward in case an individual was euthanized before end of study. (n = 8 per group; data represent mean ± SEM). One-way ANOVA with Dunnett's multiple comparisons test, $*P < 0.05$. (*F–I*) Normalized tumor growth per mouse in each treatment group. Death markers indicate reason of an individual's killing.

Discussion

KRAS is the most commonly mutated oncogene in cancer and has proven to be notoriously difficult to drug with conventional small molecules due to its shallow surface lacking easy to target binding pockets (48). Here, we show that we can inactivate KRAS through protein misfolding by TPA using synthetic amyloidogenic peptides called Pept-ins. This approach is orthogonal to classical approaches in the sense that it does not require classical surface binding pockets but depends on the availability of another class of protein interaction sites, i.e., aggregation-prone segments or APRs within the primary sequence of the protein. APRs normally participate in the folding and stabilization of the native state (5, 49). Protein misfolding and aggregation results from the self-association of such APRs into beta-sheet structured amyloid-like assemblies can be induced by synthetic amyloid peptides called Pept-ins another binding mode, which exploits the self-interacting properties of aggregating protein sequences (6–7, 8, 34, 37–54).

Recent advances in direct targeting of KRAS have yielded the discovery of KRAS G12C covalent inhibitors that are currently being used in the clinic to treat patients with advanced nonsmall cell lung cancer (55–57). Despite being a major breakthrough, many patients with different KRAS mutants do not respond to this therapy or responding patients acquire resistance over time, a recurring issue with many targeted therapies (58, 59). Being a high-value target in oncology, many novel direct KRAS-targeting therapies and technologies are currently being investigated. These include the use of RAS-binding domains (60) and KRAS degraders (41, 61). Other efforts include indirect approaches such as SOS- (62) and SHP2 (63) inhibitors, siRNA (64), vaccines (65) and cell-based therapies (65). Here, we present a KRAS-targeting moiety derived from APRs in the protein. Rather than targeting surface binding we here exploit another binding mode, which exploits the self-interacting properties of aggregating protein sequences.This approach starts from an in silico analysis of the protein's primary amino acid sequence and subsequent in silico design of synthetic peptides that contain the identified (partial) APR (Pept-ins™). Our results show that KRAS, like many proteins in the cell, is living on the edge of solubility (66). We demonstrate that specific Pept-in aggregates can push the oncoprotein over the edge into amyloid dye-binding aggregates in vitro. The Pept-ins are also readily taken up by cancer cells where they show target engagement and subsequent transition of soluble to insoluble cellular KRAS. Interestingly, little effect was observed on downstream signaling via ERK in the MAPK pathway. A previous study has shown that aggregation can trigger a cellular heat shock response and activate MAPK pathway signaling (43). Although we did not observe consistent ERK activation, we speculate that temporal cellular responses to aggregates (Pept-in and/or endogenous KRAS) can induce ERK activation. Importantly, we demonstrate that Pept-in treatment of lung cancer cells affects KRAS downstream signaling via a downregulation of the PI3K-Akt pathway and induction of apoptosis. The PI3K-Akt pathway is commonly activated in mutant KRAS-driven tumors, and its inhibition leads to tumor regression (67, 68). A wide range of cancer cell lines is sensitive to Pept-in-induced KRAS aggregation and can effectively be killed in a dose-responsive manner. Although these specific Pept-in designs showed preferential binding to mutant KRAS in cell-free studies, endogenous KRAS in RAS-dependent MEF cells and pI3K-Akt inactivation in cancer cells, this mutant specificity did not translate to selective toxicity toward mutant-KRAS cell lines in 3D cultures when cell death is measured after 5 d.

Finally, we showed in vivo efficacy in a preclinical murine lung cancer model. Daily subcutaneous administration of Pept-in resulted in significant abrogation of KRAS-driven tumor growth compared with vehicle treatment. Importantly, these fully immunocompetent mice did not show side effects, a risk that is often associated with an adverse immune reaction to protein and peptide drugs (69). It remains unclear how this result is to be connected to the in vitro toxicity study, e.g., Pept-in properties such a their cationic nature may favor tumor-specific accumulation in vivo, but further studies are needed to fully understand this.

In conclusion, TPA is an unconventional therapeutic approach that might open up part of the estimated 85% of proteins that are "undruggable" with conventional small molecules (70). Our results demonstrated proof-of-concept that the undruggable oncoprotein KRAS is a suitable TPA hit candidate. Although further study is required to improve Pept-in efficacy and limit off-target effects in cells, these Pept-ins offer an excellent basis for mutant-specific or pan-KRAS therapeutics and a rationale to expand this technology to other undruggable proteins.

Materials and Methods

Detailed description of *Materials and Methods* can be found in *SI Appendix*. All reagents, antibodies, cell lines, and other materials used are listed in the resources sheet. Statistical analyses were performed using Graphpad Prism (v9.3.1) or R (v3.6). Sample sizes are indicated in the specific figures. Experiments were replicated in at least three experiments, unless stated otherwise. Representative blots and images of one experiment are shown in the manuscript.

Data, Materials, and Software Availability. All study data are included in the article and/or *SI Appendix*.

ACKNOWLEDGMENTS. The Switch Laboratory was supported by the Flanders Institute for Biotechnology (VIB, grant no. C0401 to F.R. and J.S.); KU Leuven (Postdoctoral Mandate PDMT2/22/059 to K.K.); the Stichting Tegen Kanker [FAF-F/201//1174]; and the Fund for Scientific Research Flanders (FWO, project grants G045920N to J.S. and G0C3522N to F.R., infrastructure grants AH2016.133 to F.R. and I005022N to J.S., PhD fellowship 1S04019N to K.J., and postdoctoral fellowships 1231021N to Lad.K., 12S3722N to B.H., 12P0922N to N.L.). The authors want to thank the Flanders Innovation and Entrepreneurship (VLAIO) [HBC.2018.0407 and HBC.2020.2112] for financial support. We would also like to thank the VIB Bioimaging core for training, technical support and access to the instrument park. The authors gratefully acknowledge the Electron Microscopy Platform & the Screening Core/C-BIOS facility of the VIB – KU Leuven Center for Brain & Disease Research for their support & assistance in this work. We would like to thank the VIB Fluorescence-Activated Cells Sorting (FACS) Expertise Center and Jochen Lamote for training, technical support and access to the instruments. We would like to thank Victor Terrier, Xavier Vila Farrés, Linde Vermeylen, Eline Swinnen and Andreas Rybka for the synthesis of the biotinylated and FITC Pept-ins and Sarah Melhaoui and Jana Bruyland for their help with the cell viability assays. We would like to thank Hans Ulrichts and Rie Schultz Hansen for reading and providing constructive input for the manuscript. We would like to thank prof. dr. Tassos Economou and Lily Karamanou from the lab of Molecular Bacteriology (Rega institute, KU Leuven) for support and access to the Circular Dichroism equipment. We would also like to thank prof. dr. Ina Vorberg for kindly providing us with the N2a cells expressing GFP-labelled Sup35NM.

Author affiliations: [a]Switch Laboratory, VIB-KU Leuven Center for Brain and Disease Research, 3000 Leuven, Belgium; [b]Switch Laboratory, Department of Cellular and Molecular Medicine, KU Leuven 3000, Leuven, Belgium; [c]Aelin Therapeutics, 3001 Leuven, Belgium; [d]Experimental Oncology Group, Molecular Oncology Program, Centro Nacional de Investigaciones Oncológicas, Madrid 28029, Spain; [e]Department of Biochemistry and Molecular Biology, Faculty of Pharmacy, Complutense University, 28040 Madrid, Spain; and [f]Centro de Investigación Biomédica en Red de Cáncer (CIBERONC), Instituto de Salud Carlos III, Madrid 28029, Spain

Author contributions: K.J., F.C., V.L.W., B.S., E.B., J.S., and F.R. designed research; K.J., F.C., D.V.d.V., V.L.W., B.H., Y.L., M.N., Laleh K., Ladan K., N.L., R.v.d.K., J.V., M.R., K.K., K.M. and R.D.-R. performed research; Y.L., M.N., T.G., K.M., M.M. and M.B. contributed new reagents/analytic tools; K.J., F.C., V.L.W., N.L., R.v.d.K., M.R., B.S., J.S., and F.R. analyzed data; and K.J., N.L., J.S., and F.R. wrote the paper.

Competing interest statement: The authors have organizational affiliations and stock ownership to disclose F.R. and J.S. are scientific founders of Aelin Therapeutics and members of its scientific advisory board and own stock options of Aelin Therapeutics. E.B., B.S., F.C., V.L.W. and D.V.d.V. are employees of Aelin Therapeutics and own stock options of Aelin Therapeutics. The authors have patent filings to disclose, F.R. and J.S. are listed as inventors of patents filed by VIB/KU Leuven/UGent/VUB and licensed to Aelin Therapeutics describing the TPA technology. The Pept-ins described in this manuscript are included in patents filed by Aelin Therapeutics and VIB/KU Leuven with F.C., E.B., J.S. and F.R. listed as inventors.

1. A. Esteras-Chopo, L. Serrano, M. Lopez de la Paz, The amyloid stretch hypothesis: Recruiting proteins toward the dark side. *Proc. Natl. Acad. Sci. U.S.A.* **102**, 16672–16677 (2005), 10.1073/pnas.0505905102.
2. S. Ventura *et al.*, Short amino acid stretches can mediate amyloid formation in globular proteins: The Src homology 3 (SH3) case. *Proc. Natl. Acad. Sci. U.S.A.* **101**, 7258–7263 (2004), 10.1073/pnas.0308249101.
3. C. M. Chiti, Dobson, Amyloid formation by globular proteins under native conditions. *Nat. Chem. Biol.* **5**, 15–22 (2009), 10.1038/nchembio.131.
4. M. Hartl, Hayer-Hartl, converging concepts of protein folding in vitro and in vivo. *Nat. Struct. Mol. Biol.* **16**, 574–581 (2009), 10.1038/nsmb.1591.
5. T. Langenberg *et al.*, Thermodynamic and evolutionary coupling between the native and amyloid state of globular proteins. *Cell Reports* **31** (2020), 10.1016/j.celrep.2020.03.076.
6. R. Gallardo *et al.*, De novo design of a biologically active amyloid. *Science* **354**, aah4949–4911 (2016), 10.1126/science.aah4949.
7. L. Khodaparast *et al.*, Aggregating sequences that occur in many proteins constitute weak spots of bacterial proteostasis. *Nature Communications* **1–15**, (2018), 10.1038/s41467-018-03131-0.
8. E. Michiels *et al.*, Reverse engineering synthetic antiviral amyloids. *Nat. Commun.* **11**, 2832 (2020), 10.1038/s41467-020-16721-8.
9. J. D. Harper, P. T. Lansbury, Models of amyloid seeding in Alzheimer's disease and scrapie: Mechanistic truths and physiological consequences of the time-dependent solubility of amyloid proteins. *Ann. Rev. Biochem.* **66**, 385–407 (1997), 10.1146/annurev.biochem.66.1.385.
10. A. Ganesan *et al.*, Selectivity of aggregation-determining interactions. *J. Mol. Biol.* **427**, 236–247 (2015), 10.1016/j.jmb.2014.09.027.
11. M. R. Sawaya *et al.*, Atomic structures of amyloid cross-beta spines reveal varied steric zippers. *Nature* **447**, 453–457 (2007), 10.1038/nature05695.
12. L. C. Walker, M. I. Diamond, K. E. Duff, B. T. Hyman, Mechanisms of Protein Seeding in Neurodegenerative Diseases. *JAMA Neurol.* **70**, 304 (2013), 10.1001/jamaneurol.2013.1453.
13. G. A. Hobbs, C. J. Der, K. L. Rossman, RAS isoforms and mutations in cancer at a glance. *J. Cell Sci.* **129**, 1287–1292 (2016), 10.1242/jcs.182873.
14. I. A. Prior, F. E. Hood, J. L. Hartley, The Frequency of Ras Mutations in Cancer. *Cancer Res.* **80**, 2969–2974 (2020), 10.1158/0008-5472.can-19-3682.
15. S. P. Mo, J. M. Coulson, I. A. Prior, RAS variant signalling. *Biochem. Soc. Transactions* **46**, 1325–1332 (2018), 10.1042/BST20180173.
16. A.-M. Fernandez-Escamilla, F. Rousseau, J. Schymkowitz, L. Serrano, Prediction of sequence-dependent and mutational effects on the aggregation of peptides and proteins. *Nat. Biotechnol.* **22**, 1302–1306 (2004), 10.1038/nbt1012.
17. J. A. J. Housmans, G. Wu, J. Schymkowitz, F. Rousseau, A guide to studying protein aggregation. *FEBS J.* (2021), 10.1111/febs.16312.
18. R. B. Ryan, Corcoran, Therapeutic strategies to target RAS-mutant cancers. *Nat. Rev. Clin. Oncol.* **1–12**, (2018), 10.1038/s41571-018-0105-0.
19. J. Schymkowitz *et al.*, The FoldX web server: An online force field. *Nucleic Acids Res.* **33**, W382–W388 (2005), 10.1093/nar/gki387.
20. R. van der Kant *et al.*, Prediction and reduction of the aggregation of monoclonal antibodies. *J. Mol. Biol.* **429**, 1244–1261 (2017), 10.1016/j.jmb.2017.03.014.
21. A. Ganesan *et al.*, Structural hot spots for the solubility of globular proteins. *Nat. Commun.* **7**, 10816 (2016), 10.1038/ncomms10816.
22. Van Durme *et al.*, Solubis: A webserver to reduce protein aggregation through mutation. *Protein Eng Des Sel* **29**, 285–289 (2016), 10.1093/protein/gzw019.
23. I. A. Prior, P. D. Lewis, C. Mattos, A comprehensive survey of Ras mutations in cancer. *Cancer Res.* **72**, 2457–2467 (2012), 10.1158/0008-5472.CAN-11-2612.
24. J. C. Hunter *et al.*, Biochemical and Structural Analysis of Common Cancer-Associated KRAS Mutations. *Mol. Cancer Res.* **13**, 1325–1335 (2015), 10.1158/1541-7786.MCR-15-0203.
25. R. Gupta, Mahalakshmi, Helix–strand interaction regulates stability and aggregation of the human mitochondrial membrane protein channel VDAC3. *J. General Physiol.* **151**, 489–504 (2019), 10.1085/jgp.201812272.
26. M. T. Schermeyer, A. K. Wöll, B. Kokke, M. Eppink, J. Hubbuch, Characterization of highly concentrated antibody solution - A toolbox for the description of protein long-term solution stability. *MAbs* **9**, 1169–1185 (2017), 10.1080/19420862.2017.1338222.
27. M. Rodríguez-Bolaños, H. Miranda-Astudillo, E. Pérez-Castañeda, D. González-Halphen, R. Perez-Montfort, Native aggregation is a common feature among triosephosphate isomerases of different species. *Sci. Rep.* **10**, 1338 (2020), 10.1038/s41598-020-58272-4.
28. G. Marcon, G. Plakoutsi, F. Chiti, Protein aggregation starting from the native globular state. *Methods Enzymol.* **413**, 75–91 (2006), 10.1016/s0076-6879(06)13004-9.
29. L. M. Oliveira *et al.*, Insights into the molecular mechanism of protein native-like aggregation upon glycation. *Biochim. Biophys. Acta* **1834**, 1010–1022 (2013), 10.1016/j.bbapap.2012.12.001.
30. F. Bemporad, A. De Simone, F. Chiti, C. M. Dobson, Characterizing intermolecular interactions that initiate native-like protein aggregation. *Biophys J* **102**, 2595–2604 (2012), 10.1016/j.bpj.2012.03.057.
31. A. Lamiable *et al.*, PEP-FOLD3: Faster de novostructure prediction for linear peptides in solution and in complex. *Nucleic Acids Res.* **44**, W449–W454 (2016), 10.1093/nar/gkw329.
32. A. Åslund *et al.*, Novel Pentameric Thiophene Derivatives for in Vitro and in Vivo Optical Imaging of a Plethora of Protein Aggregates in Cerebral Amyloidoses. *ACS Chem. Biol.* **4**, 673–684 (2009), 10.1021/cb900112v.
33. P. B. Stathopulos *et al.*, Sonication of proteins causes formation of aggregates that resemble amyloid. *Protein Sci.* **13**, 3017–3027 (2008), 10.1110/ps.04831804.
34. L. Khodaparast *et al.*, Bacterial protein homeostasis disruption as a therapeutic intervention. *Front. Mol. Biosci.* **8**, (2021), ARTN 681855.
35. M. R. Eisenberg, Sawaya, Structural Studies of Amyloid Proteins at the Molecular Level. *Annu. Rev. Biochem.* **86**, 69–95 (2017), 10.1146/annurev-biochem-061516-045104.
36. M. Drosten *et al.*, Genetic analysis of Ras signalling pathways in cell proliferation, migration and survival. *EMBO J.* **29**, 1091–1104 (2010), 10.1038/emboj.2010.7.
37. J. R. Couceiro *et al.*, Sequence-dependent internalization of aggregating peptides. *J. Biol. Chem.* **290**, 242–258 (2015), 10.1074/jbc.m114.586636.
38. F. U. Hartl, A. Bracher, M. Hayer-Hartl, Molecular chaperones in protein folding and proteostasis. *Nature* **475**, 324–332 (2011), 10.1038/nature10317.
39. F. J. Oliver *et al.*, Importance of poly(ADP-ribose) polymerase and its cleavage in apoptosis. Lesson from an uncleavable mutant. *J. Biol. Chem.* **273**, 33533–33539 (1998), 10.1074/jbc.273.50.33533.
40. M. R. Janes *et al.*, Targeting KRAS mutant cancers with a covalent G12C-specific inhibitor. *Cell* **172**, 578–581.e517 (2018), 10.1016/j.cell.2018.01.006.
41. N. Bery, A. Miller, T. Rabbitts, A potent KRAS macromolecule degrader specifically targeting tumours with mutant KRAS. *Nat. Commun.* **11**, (2020), 10.1038/s41467-020-17022-w.
42. A. R. Moore, S. C. Rosenberg, F. McCormick, S. Malek, RAS-targeted therapies: is the undruggable drugged?*Nat. Rev. Drug Discovery* (2020), 10.1038/s41573-020-0068-6.
43. Z. Tang *et al.*, MEK Guards Proteome Stability and Inhibits Tumor- Suppressive Amyloidogenesis via HSF1. *Cell* **160**, 729–744 (2015), 10.1016/j.cell.2015.01.028.
44. A. M. Waters *et al.*, Evaluation of the selectivity and sensitivity of isoform- and mutation-specific RAS antibodies. *Sci. Signal.* **10**, eaao3332 (2017), 10.1126/scisignal.aao3332.
45. B. B. Holmes *et al.*, Proteopathic tau seeding predicts tauopathy in vivo. *Proc. Natl. Acad. Sci. U.S.A.* **111**, E4376–4385 (2014), 10.1073/pnas.1411649111.
46. J. P. Hofmann *et al.*, Cell-to-cell propagation of infectious cytosolic protein aggregates. *Proc. Natl. Acad. Sci. U.S.A.* **110**, 5951–5956 (2013), 10.1073/pnas.1217321110.
47. E. L. Jackson *et al.*, The Differential Effects of Mutant p53 Alleles on Advanced Murine Lung Cancer. *Cancer Res.* **65**, 10280–10288 (2005), 10.1158/0008-5472.can-05-2193.
48. C. V. Dang, E. P. Reddy, K. M. Shokat, L. Soucek, Drugging the "undruggable" cancer targets. *Nat Rev Cancer* **17**, 502–508 (2017), 10.1038/nrc.2017.36.
49. B. Houben, F. Rousseau, J. Schymkowitz, Protein structure and aggregation: a marriage of necessity ruled by aggregation gatekeepers. *Trends Biochem. Sci.* **47**, 194–205 (2022), 10.1016/j.tibs.2021.08.010.
50. G. Wu *et al.*, Investigating the mechanism of action of aggregation-inducing antimicrobial Pept-ins. *Cell Chem. Biol.* **28**, 524–536.e524 (2021), 10.1016/j.chembiol.2020.12.008.
51. M. Siemons *et al.*, Synthetic Pept-Ins as a Generic Amyloid-Like Aggregation-Based Platform for In Vivo PET Imaging of Intracellular Targets. *Bioconjug. Chem.* **32**, 2052–2064 (2021), 10.1021/acs.bioconjchem.1c00369.
52. C. Betti, J. Schymkowitz, F. Rousseau, E. Russinova, Selective Knockdowns in Maize by Sequence-Specific Protein Aggregation. *Methods Mol. Biol.* **1676**, 109–127 (2018), 10.1007/978-1-4939-7315-6_6.
53. C. Betti *et al.*, Sequence-specific protein aggregation generates defined protein knockdowns in plants. *Plant Physiol.*, 00335.02016-00315 (2016), 10.1104/pp.16.00335.
54. N. G. Bednarska *et al.*, Protein aggregation as an antibiotic design strategy. *Mol. Microbiol.* **99**, 849–865 (2015), 10.1111/mmi.13269.
55. F. Skoulidis *et al.*, Sotorasib for Lung Cancers with KRAS p. G12C Mutation. *N. Engl. J. Med.* **384**, 2371–2381 (2021), 10.1056/nejmoa2103695.
56. J. Hallin *et al.*, The KRASG12CInhibitor MRTX849 Provides Insight toward Therapeutic Susceptibility of KRAS-Mutant Cancers in Mouse Models and Patients. *Cancer Discovery* **10**, 54–71 (2020), 10.1158/2159-8290.CD-19-1167.
57. J. Canon *et al.*, The clinical KRAS(G12C) inhibitor AMG 510 drives anti-tumour immunity. *Nature* **1–26**, (2019), 10.1038/s41586-019-1694-1.
58. M. M. Awad *et al.*, Acquired Resistance to KRASG12C Inhibition in Cancer. *New Engl. J. Medicine* **384**, 2382–2393 (2021), 10.1056/nejmoa2105281.
59. J. Y. Xue *et al.*, Rapid non-uniform adaptation to conformation-specific KRAS(G12C) inhibition. *Nature* **1–23**, (2020), 10.1038/s41586-019-1884-x.
60. T. K. Nomura *et al.*, Specific inhibition of oncogenic RAS using cell-permeable RAS-binding domains. *Cell Chem. Biol.*, (2021), 10.1016/j.chembiol.2021.04.013.
61. M. J. Bond, L. Chu, D. A. Nalawansha, K. Li, C. M. Crews, Targeted Degradation of Oncogenic KRASG12C by VHL-Recruiting PROTACs. *ACS Central Sci.* **6**, 1367–1375 (2020), 10.1021/acscentsci.0c00411.
62. M. H. Hofmann *et al.*, BI-3406, a Potent and Selective SOS1–KRAS Interaction Inhibitor, Is Effective in KRAS-Driven Cancers through Combined MEK Inhibition. *Cancer Discovery* **11**, 142–157 (2021), 10.1158/2159-8290.cd-20-0142.
63. S. Mainardi *et al.*, SHP2 is required for growth of KRAS-mutant non-small-cell lung cancer in vivo. *Nat. Medicine* **24**, 961–967 (2018), 10.1038/s41591-018-0023-9.
64. M. S. Strand *et al.*, Precision delivery of RAS-inhibiting siRNA to KRAS driven cancer via peptide-based nanoparticles. *Oncotarget* **10**, 4761–4775 (2019), 10.18632/oncotarget.27109.
65. C. A. Arbelaez *et al.*, A nanoparticle vaccine that targets neoantigen peptides to lymphoid tissues elicits robust antitumor T cell responses. *npj Vaccines* **5**, (2020), 10.1038/s41541-020-00253-9.
66. G. Vecchi *et al.*, Proteome-wide observation of the phenomenon of life on the edge of solubility. *Proc. Natl. Acad. Sci. U.S.A.* **117**, 1015–1020 (2020), 10.1073/pnas.1910444117.
67. E. Castellano *et al.*, Requirement for Interaction of PI3-Kinase p110α with RAS in Lung Tumor Maintenance. *Cancer Cell* **24**, 617–630 (2013), 10.1016/j.ccr.2013.09.012.
68. J. Castellano, Downward, RAS Interaction with PI3K: More Than Just Another Effector Pathway. *Genes. amp Cancer* **2**, 261–274 (2011), 10.1177/1947601911408079.
69. V. Jawa *et al.*, T-Cell Dependent Immunogenicity of Protein Therapeutics Pre-clinical Assessment and Mitigation-Updated Consensus and Review 2020. *Front. Immunol.* **11**, 1301 (2020), 10.3389/fimmu.2020.01301.
70. T. K. Neklesa, J. D. Winkler, C. M. Crews, Targeted protein degradation by PROTACs. *Pharmacol. Therapeutics* **174**, 138–144 (2017), 10.1016/j.pharmthera.2017.02.027.